Rapid Communications

Gate-tunable infrared plasmons in electron-doped single-layer antimony

D. A. Prishchenko,[1,*] V. G. Mazurenko,[1] M. I. Katsnelson,[1,2] and A. N. Rudenko[3,1,2]

[1]*Theoretical Physics and Applied Mathematics Department, Ural Federal University, Mira Street 19, 620002 Ekaterinburg, Russia*

[2]*Institute for Molecules and Materials, Radboud University, Heijendaalseweg 135, 6525 AJ Nijmegen, The Netherlands*

[3]*School of Physics and Technology, Wuhan University, Wuhan 430072, China*

(Received 6 September 2018; revised manuscript received 11 October 2018; published 9 November 2018)

We report on a theoretical study of collective electronic excitations in single-layer antimony crystals (antimonene), a novel two-dimensional semiconductor with strong spin-orbit coupling. Based on a tight-binding model, we consider electron-doped antimonene and demonstrate that the combination of spin-orbit effects with an external bias gives rise to peculiar plasmon excitations in the midinfrared spectral range. These excitations are characterized by low losses and negative dispersion at frequencies effectively tunable by doping and bias voltage. The observed behavior is attributed to the spin splitting of the conduction band, which induces interband resonances, affecting the collective excitations. Our findings open up the possibility to develop plasmonic and optoelectronic devices with high tunability, operating in a technologically relevant spectral range.

DOI: 10.1103/PhysRevB.98.201401

The growing field of plasmonics continues to gather attention from the material science community. Collective oscillations of electron density provide a way to couple indecent electromagnetic radiation to matter, which enables one to confine and enhance the local field inside the material, essentially turning the optical signal into an electrical signal. Their practical use is diverse and depends on the desirable frequency region. The related fields include biosensing, light harvesting, optical thermal heating, lasers, photodetection, and others [1–7]. Wavelengths in the midinfrared (IR) spectral range are especially attractive as as they offer a large set of unique and technologically relevant applications [8].

Among the diverse plasmonic materials, two-dimensional (2D) structures stand out as especially appealing candidates for plasmonics [9–12]. For example, graphene, the most known 2D material, exhibits unique optoelectronic properties in many ways, showing high-energy confinement and large tunability [13–23]. Intensive research has also been focused on other two-dimensional materials. Among them are transition-metal dichalcogenides and black phosphorus [24–29]. The former exhibits plasmon resonances in the visible and near ultraviolet ranges, while the latter demonstrates strongly anisotropic optical properties, which makes it suitable for hosting hyperbolic plasmons [30]. On the other hand, emerging 2D materials with magnetic degrees of freedom [31,32] open up another exciting direction in the field of nanoplasmonics [33].

In this Rapid Communication, we study plasmon excitations in electron-doped single-layer antimony (SL-Sb), a recently fabricated 2D semiconductor with remarkable environmental stability [34,35], and presumably high carrier mobility [36]. The electronic structure of SL-Sb is strongly influenced by the spin-orbit interaction (SOI) [37,38], which presumes additional functionalities and control. We find that under application of the gate voltage, electron-doped SL-Sb demonstrates unusual low-loss plasmonic excitations in the mid-IR region. The observed excitations are characterized by a negative dispersion at small wave vectors, and turn out to be highly tunable by either a bias potential or charge doping. The effect mainly originates from the SOI-induced spin splitting of the conduction band, resulting in interband resonances, significantly affecting the dielectric response.

Antimonene has a hexagonal $A7$-type crystal structure (space group D^3_{3d}) with a lattice parameter $a = 4.12$ Å and two sublattices displaced vertically by $b = 1.65$ Å [38]. SL-Sb is predicted to be an indirect gap semiconductor with the gap in the near-IR range [39]. The electronic structure of SL-Sb can be accurately described over a wide energy range using a tight-binding (TB) model proposed in Ref. [38]. The model is defined in the basis of p orbitals and explicitly takes into account SOI. In the presence of a vertical bias the corresponding Hamiltonian has the following form,

$$H = \sum_{ij\sigma\sigma'} t_{ij}^{\sigma\sigma'} c_{i\sigma}^{\dagger} c_{j\sigma'} + \frac{V}{d} \sum_{i\sigma} z_i c_{i\sigma}^{\dagger} c_{i\sigma}, \qquad (1)$$

where $c_{i\sigma}^{\dagger}$ ($c_{j\sigma'}$) is the creation (annihilation) operator of electrons with spin σ (σ') at orbital i (j), z_i is the z component of the position operator of the orbital i, $t_{ij}^{\sigma\sigma'}$ is the spin-dependent matrix of hopping integrals, V is the bias voltage applied to the upper and lower planes of the system, and d is the vertical displacement between the sublattices [Fig. 1(d)].

Figure 1(a) shows the energy dispersion and density of states (DOS) of the conduction states of SL-Sb. The conduction-band minimum corresponds to a low-symmetry Σ point (C_{2v} point group), which is located at 0.56 Å^{-1} from the Γ point along the Γ-M direction of the Brillouin zone. Low-energy dispersion at the band edge can be described by two effective masses, $m_{\Sigma}^{\parallel} = 0.43m_0$ and $m_{\Sigma}^{\perp} = 0.13m_0$, corresponding to the direction along and perpendicular to Γ-M,

*d.a.prishchenko@urfu.ru

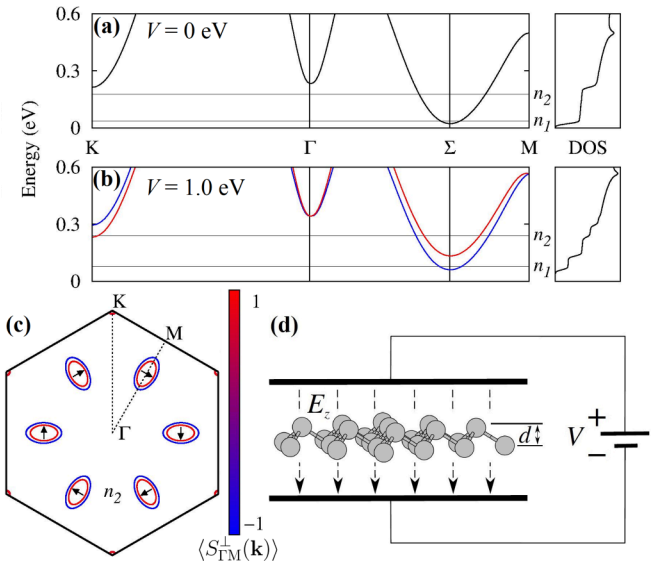

FIG. 1. Band structure and density of states of SL-Sb calculated (a) in the absence of and (b) in the presence of a vertical bias with $V = 1$ eV. In each case, the black horizontal line marks the Fermi energy corresponding to the electron doping with concentrations $n_1 = 10^{13}$ and $n_2 = 10^{14}$ cm^{-2}. (c) Fermi-surface contour for the concentration n_2 and bias potential $V = 1$ eV, with colors corresponding to the expectation value (in units of $\hbar/2$) of the spin operator projected on the direction perpendicular to Γ-M, $S^{\perp}_{\Gamma M}(\mathbf{k})$. Blue corresponds to the clockwise direction, while red is for the anticlockwise direction. The direction of the total spin per valley is shown by the black arrows. (d) Schematic representation of SL-Sb embedded in the electric field controlled by the gate voltage.

respectively. This gives rise to six ellipsoidal valleys formed around the zone center. In the presence of a vertical bias (or perpendicular static electric field), the spin degeneracy is lifted as a result of inversion symmetry breaking [40]. The resulting spin splitting is shown in Fig. 1(b), which reaches 0.1 eV at the bias voltage $V = 1$ eV. In this situation, the effective masses enhance to $m^{\parallel}_{\Sigma} = 0.47m_0$ and $m^{\perp}_{\Sigma} = 0.17m_0$ for both bands. The corresponding Fermi energy contours are shown in Fig. 1(c), where projections on the opposite spin directions are shown by color. The splitting of electron states in SL-Sb is different from the Rashba splitting typical for narrow gap 2D electron gas, but rather resembles exchange splitting in the ferromagnets [41]. Indeed, the expectation value of the spin operator projected to the direction perpendicular to Γ-M, $\langle S^{\perp}_{\Gamma M}(\mathbf{k})\rangle = \langle\psi^{\sigma}_i(\mathbf{k})|S^{\perp\sigma\sigma'}_{\Gamma M}|\psi^{\sigma'}_i(\mathbf{k})\rangle$, shows that the two states within each valley correspond to opposite ($\pm\hbar/2$) spin projections [see Fig. 1(c)]. In contrast to ferromagnets, time-reversal symmetry is preserved in biased SL-Sb, leading to zero net magnetization.

The combination of a gate-controlled band splitting and finite DOS at the Fermi energy achievable by doping opens up the possibility to tune plasmonic resonances in SL-Sb, which is of interest for practical applications. Here, we restrict ourselves to the case of electron doping only, as it represents the most interesting case. We only note that the properties of hole-doped SL-Sb can be described with high accuracy by the well-studied Rashba model [42].

To investigate the optical properties of SL-Sb, we first calculate the frequency-dependent dielectric matrix $\epsilon^{(\mathbf{q})}_{ij}(\omega)$. To this end, we use the random phase approximation assuming no dielectric background (free-standing sample),

$$\epsilon^{(\mathbf{q})}_{\sigma\sigma'}(\omega) = \delta_{\sigma\sigma'} - \frac{2\pi e^2}{qS}\Pi^{(\mathbf{q})}_{\sigma\sigma'}(\omega), \tag{2}$$

where $2\pi e^2/qS$ is the long-wavelength approximation of the bare Coulomb interaction density in 2D, and $\Pi^{(\mathbf{q})}_{\sigma\sigma'}(\omega)$ is the polarizability matrix. For the purpose of our study it is sufficient to ignore the local field effects related to the orbital degrees of freedom, while the effects of the spin subsystem turn out to be important. Using the definition given above, the spectrum of plasma excitations is determined by the equation $\det[\epsilon^{(\mathbf{q})}_{\sigma\sigma'}(\omega_p)] = i\gamma^{(\mathbf{q})}(\omega_p)$, where $\gamma^{(\mathbf{q})}(\omega_p)$ is the damping factor, and $\omega_p = \omega^{(\mathbf{q})}_p$ is the plasma frequency. In the spinor basis, the polarizability can be defined as [43]

$$\Pi^{(\mathbf{q})}_{\sigma\sigma'}(\omega) = \sum_{\substack{ij\mathbf{k}\\mn}} \left(f^{(\mathbf{k})}_m - f^{(\mathbf{k}')}_n\right)\frac{C^{(\mathbf{k})}_{i\sigma m}C^{*(\mathbf{k}')}_{i\sigma n}C^{*(\mathbf{k})}_{j\sigma' m}C^{(\mathbf{k}')}_{j\sigma' n}}{E^{(\mathbf{k})}_m - E^{(\mathbf{k}')}_n + \omega + i\eta}, \tag{3}$$

where $C^{(\mathbf{k})}_{i\sigma m}$ is the contribution of the ith orbital $w^{\mathbf{R}}_{i\sigma}(\mathbf{r})$ with spin σ to the Hamiltonian eigenstate $\psi^{\mathbf{k}}_m(\mathbf{r}) = \sum_{i\sigma\mathbf{R}} C^{(\mathbf{k})}_{i\sigma m}e^{i\mathbf{k}\cdot\mathbf{R}}w^{\mathbf{R}}_{i\sigma}(\mathbf{r})$ with energy $E^{(\mathbf{k})}_m$, $\mathbf{k}' = \mathbf{k} + \mathbf{q}$, $f^{(\mathbf{k})}_m = \{\exp[(E^{(\mathbf{k})}_m - \mu)/T] + 1\}^{-1}$ is the Fermi-Dirac occupation factor, μ is the chemical potential determined by the carrier concentration n, and η is a broadening term. In our calculations, we used $T = 300$ K, $\eta = 5$ meV, and two representative values of electron doping, $n = 10^{13}$ and 10^{14} cm^{-2}. Brillouin zone integration has been performed on a grid of $\sim 10^6$ $\mathbf{k}$ points.

To understand the extent to which one can tune the optical properties of SL-Sb, we calculate the plasmon loss function $L(\mathbf{q},\omega) = \mathrm{Im}\{1/\det[\epsilon^{(\mathbf{q})}_{\sigma\sigma'}(\omega)]\}$, and study its behavior with respect to the carrier doping and external potential strength. The results are presented in Fig. 2, which also shows boundaries of the particle-hole continuum $\omega^{(\mathbf{q})}_0$. In the absence of an external potential the electrons occupy the bottom of a single parabolic band with no interband transition allowed [see Fig. 1(a)]. In this situation, the optical response is determined by the plasma oscillations of the nonrelativistic 2D electron gas, for which one has $\omega^2_p \approx an|\mathbf{q}| + bE_Fq^2$, where a and b are constants, and E_F is the Fermi energy [44]. The corresponding loss functions for $n = 10^{13}$ and 10^{14} cm^{-2} are shown in Figs. 2(a) and 2(c), from which one can see a "classical" $\sqrt{q}$ plasmon dispersion at low frequencies. At $\omega^{(\mathbf{q})}_p < \omega^{(\mathbf{q})}_0$ the plasmon dispersion enters a single-particle excitation continuum and decays into electron-hole pairs. The energy scale of the phonon excitations in SL-Sb lies in the far-IR region [40], meaning the absence of phonon-plasmon resonances [45] in the relevant spectral range.

The plasmon spectrum changes drastically when we introduce an external bias potential with magnitude 1 eV [see Figs. 2(b) and 2(d)]. In this case, a second ("optical") plasmon branch appears. This branch has a large spectral weight and lies in the mid-IR region, independently of the electron concentrations considered. These excitations have a peculiar

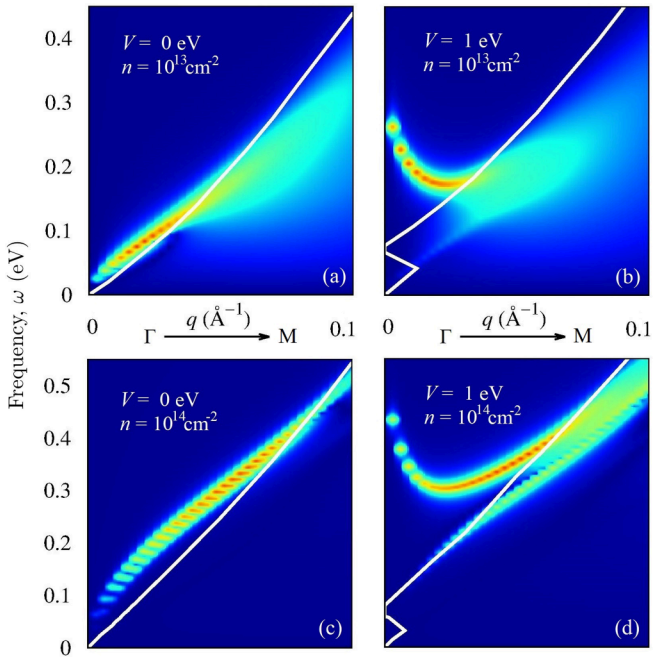

FIG. 2. Plasmon loss function $L(\mathbf{q},\omega)$ in SL-Sb calculated for electron doping concentrations $n = 10^{13}$ and 10^{14} cm^{-2} (top and bottom panels), and bias voltages $V = 0$ and 1 eV (left and right panels). The white line represents boundaries of the particle-hole continuum determined by the poles of the polarization function [Eq. (3)], $\omega_0^{(\mathbf{q})} = \max\{E_n^{(\mathbf{k}+\mathbf{q})} - E_m^{(\mathbf{k})}\}$.

paraboliclike negative dispersion at small q. Their origin is related to the SOI-mediated splitting of the conduction band [Fig. 1(b)] allowing for the interband transitions, reminiscent

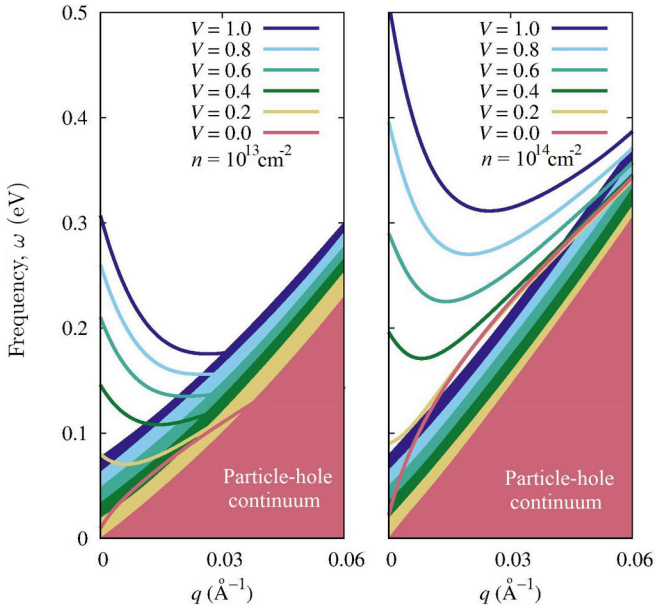

FIG. 3. Solutions of the equation $\mathrm{Re}\{\det[\epsilon^{(\mathbf{q})}_{\sigma\sigma'}(\omega_p)]\} = 0$, determining lossless plasmon modes calculated for different bias potentials V (in eV), and for two representative values of electron doping n in SL-Sb. The corresponding region of Landau damping is shown in each case by the same color. For clarity, only the highest ("optical") plasmon mode is shown at each gate voltage.

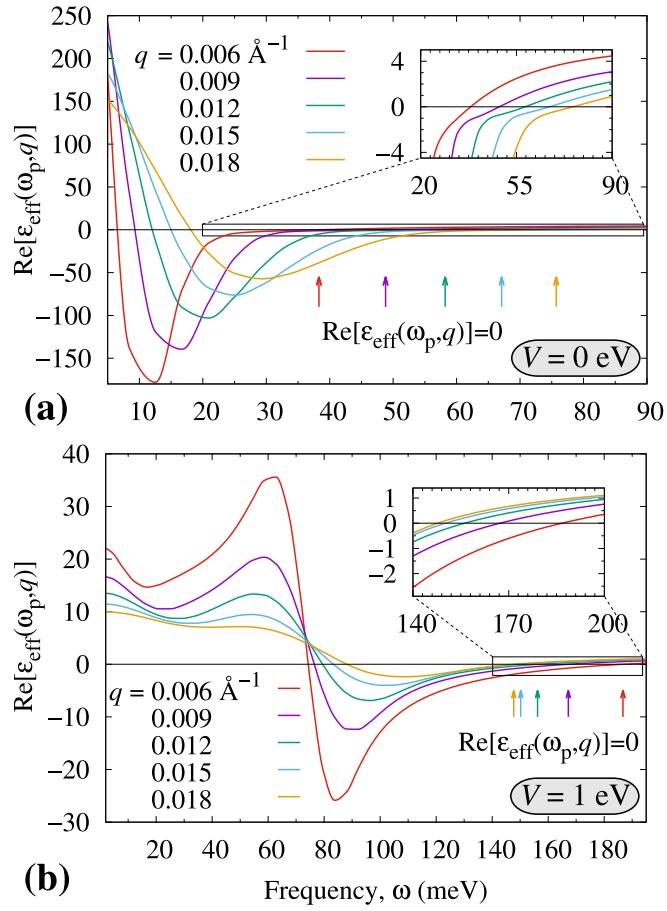

FIG. 4. Frequency dependence of $\mathrm{Re}[\epsilon_{\mathrm{eff}}(\omega, q)]$ in SL-Sb calculated for a series of $\mathbf{q}$ points along the Γ-M path. (a) and (b) correspond to $V = 0$ and $V = 1$ eV, respectively. In both cases, an electron doping of 10^{13} cm^{-2} is assumed. The inset shows a zoom-in of the region where $\mathrm{Re}[\epsilon_{\mathrm{eff}}(\omega, q)] = 0$, determining the "optical" plasmon modes. Arrows point to the corresponding solutions for the given set of $\mathbf{q}$ points.

of that in bilayer graphene [45,46]. The frequency of the excitations at small q can be effectively tuned by the gate voltage, as it is shown in Fig. 3. Depending on the level of electron doping (10^{13} or 10^{14} cm^{-2}), one can smoothly tune $\omega_p(q \to 0)$ from 0 to 0.3 (or 0.5) eV by applying bias voltage in the range up to 1 eV. In all cases the relevant excitations lie above the Landau damping region ($\omega_p > \omega_0$), indicating fully coherent plasmon modes. On the contrary, the "classical" plasmon mode in biased SL-Sb falls inside the particle-hole continuum, and turns out to be essentially damped. As a consequence of the Kramers-Kronig sum rule [47], the entire spectral weight at long wavelengths is transferred to the "optical" mode. We note that further tunability toward lower frequencies can be achieved by the dielectric substrate (not considered here).

To gain further insights into the origin of plasma excitations in SL-Sb, we analyze the effective dielectric functions $\epsilon^{(\mathbf{q})}_{\mathrm{eff}}(\omega) = \det[\epsilon^{(\mathbf{q})}_{\sigma\sigma'}(\omega)]$, shown in Fig. 4 for $n = 10^{13}$ cm^{-2}. Without a bias potential [Fig. 4(a)] one has the typical behavior $\epsilon_{\mathrm{eff}}(\omega) \approx 1 - \omega_p^2/(\omega^2 + i\omega\gamma)$ at large enough frequencies with $\omega_p^2 \sim q$. At $\omega < \omega_p$ there is another solution of the

equation $\mathrm{Re}[\epsilon_{\mathrm{eff}}^{(\mathbf{q})}(\omega)] = 0$ with $\omega \sim q$. This solution is known as the "acoustic" plasmon mode corresponding to out-of-phase charge density oscillations observed in 2D materials with a finite thickness, including bilayer graphene [48], transition-metal dichalcogenides [49], and phosphorene [50]. Similar to the other systems, this mode is strongly damped as it lies in the particle-hole continuum. If we introduce the bias potential [Fig. 4(b)], $\epsilon_{\mathrm{eff}}(\omega)$ exhibits a discontinuity at $\omega = \omega_0(V)$, and has the characteristic shape typical of a conductor with resonant scatterers [51],

$$\epsilon_{\mathrm{eff}}(\omega) \approx 1 - \sum_l \frac{\omega_{p,l}^2}{\omega^2 - \omega_{0,l}^2 + i\omega\gamma_l}, \tag{4}$$

where l denotes different scattering channels, which in our case can be associated with intraband and interband transitions. Equation (4) allows for the existence of plasmons with negative dispersion if there is l for which $\partial\omega_{0,l}^2/\partial q < 0$. As can be seen from Figs. 2(b) and 2(d), this condition is fulfilled in biased SL-Sb at $q \lesssim 0.02$ Å^{-1}, which coincides with the region of negative plasmon dispersion. Apart from this prominent solution, there is an overdamped plasmon mode at frequencies close to the interband resonance [Fig. 4(b)], while the "acoustic" branch turns out to be fully suppressed at large enough V.

Plasmon excitations with negative dispersion is an uncommon but not unique phenomenon. It first appeared in the context of bulk Cs crystal [52], but was further observed in other materials [53,54]. A recent study reports similar behavior in electron-doped monolayer MoS_2 [55]. Negative dispersion is associated with negative group velocity, indicating a negative energy flux. This phenomenon gives rise to an intriguing subfield of nanoplasmonics with a number of exotic optical effects including a negative refraction index [56–58]. The fact that the corresponding frequencies in SL-Sb fall in the technologically relevant spectral range makes this system prospective for further experimental studies. Plasmons in 2D systems can be accessed by a variety of methods, including electron energy-loss spectroscopy [13], IR optical measurements [15], and scanning probe microscopy [17], performed earlier for graphene. The high tunability of plasmon excitations in SL-Sb offered by the strong SOI is another appealing aspect to be explored in the context of nanoplasmonic applications. To experimentally observe the peculiar character of plasmons in SL-Sb, strong electric fields on the order of 0.1–0.5 eV/Å may be required. This can be achieved, for example, by the encapsulation of SL-Sb in polar semiconductors [59], or by means of heavy alkali-metal doping [60].

To conclude, we theoretically studied optoelectronic properties of SL-Sb at realistic electron concentrations by varying the applied gate voltage. In addition to the classical 2D plasmon, we find that SOI-induced spin splitting gives rise to a different lossless plasmon branch in the mid-IR region at frequencies highly sensitive to the bias voltage. Remarkably, these excitations exhibit negative dispersion in a wide range of wave vectors. This behavior is attributed to the strong SOI and inversion symmetry breaking, and indicates as well the important role of the local field effects in the spin channel. Our findings suggest SL-Sb to be an appealing nanoplasmonic material with great gate tunability, which paves the way for further experimental and theoretical studies in this field.

This work was supported by the Russian Science Foundation Grant No. 17-72-20041. Part of the research was carried out using the high-performance computing resources at Moscow State University [61].

[1] S. A. Maier, *Plasmonics: Fundamentals and Applications* (Springer, New York, 2007).
[2] W. A. Murray and W. L. Barnes, Plasmonic materials, Adv. Mater. **19**, 3771 (2007).
[3] S. V. Boriskina, H. Ghasemi, and G. Chen, Plasmonic materials for energy: From physics to applications, Mater. Today **16**, 375 (2013).
[4] K. Kneipp, Y. Wang, H. Kneipp, L. T. Perelman, I. Itzkan, R. R. Dasari, and M. S. Feld, Single Molecule Detection Using Surface-Enhanced Raman Scattering (SERS), Phys. Rev. Lett. **78**, 1667 (1997).
[5] K. M. Mayer and J. H. Hafner, Localized surface plasmon resonance sensors, Chem. Rev. **111**, 3828 (2011).
[6] D. Rodrigo, O. Limaj, D. Janner, D. Etezadi, F. J. García de Abajo, V. Pruneri, and H. Altug, Mid-infrared plasmonic biosensing with graphene, Science **349**, 165 (2015).
[7] V. J. Sorger, R. F. Oulton, R.-M. Ma, and X. Zhang, Toward integrated plasmonic circuits, MRS Bull. **37**, 728 (2012).
[8] Y. Zhong, S. D. Malagari, T. Hamilton, and D. M. Wasserman, Review of mid-infrared plasmonic materials, J. Nanophoton. **9**, 093791 (2015).
[9] T. Low, A. Chaves, J. D. Caldwell, A. Kumar, N. X. Fang, P. Avouris, T. F. Heinz, F. Guinea, L. Martin-Moreno, and F. Koppens, Polaritons in layered two-dimensional materials, Nat. Mater. **16**, 182 (2016).
[10] Y. Li, Z. Li, C. Chi, H. Shan, L. Zhen, and Z. Fang, Plasmonics of 2D nanomaterials: Properties and applications, Adv. Sci. **4**, 1600430 (2018).
[11] H. Pfnür, C. Tegenkamp, and L. Vattuone, Plasmons in one and two dimensions, in *Springer Handbook on Surface Science*, edited by M. Rocca, T. Rahman, and L. Vattuone (Springer, Heidelberg, 2017).
[12] A. Agarwal, M. S. Vitiello, L. Viti, A. Cupolillo, and A. Politano, Plasmonics with two-dimensional semiconductors: From basic research to technological applications, Nanoscale **10**, 8938 (2018).
[13] M. H. Gass, U. Bangert, A. L. Bleloch, P. Wang, R. R. Nair, and A. K. Geim, Free-standing graphene at atomic resolution, Nat. Nanotechnol. **3**, 676 (2008).
[14] F. H. L. Koppens, D. E. Chang, and F. J. García de Abajo, Graphene plasmonics: A platform for strong light–matter interactions, Nano Lett. **11**, 3370 (2011).
[15] Z. Fei, G. O. Andreev, W. Bao, L. M. Zhang, A. S. McLeod, C. Wang, Z. Zhao, G. Dominguez, M. Thiemens, M. M. Fogler, M. Tauber, A. Castro-Neto, C. N. Lau, F. Keilmann, and D. N. Basov, Infrared nanoscopy of Dirac plasmons at the graphene-SiO_2 interface, Nano Lett. **11**, 4701 (2011).

[16] J. Chen, M. Badioli, P. Alonso-González, S. Thongrattanasiri, F. Huth, J. Osmond, M. Spasenovic, A. Centeno, A. Pesquera, P. Godignon, A. Zurutuza Elorza, N. Camara, F. J. G. de Abajo, R. Hillenbrand, and F. H. L. Koppens, Optical nano-imaging of gate-tunable graphene plasmons, Nature (London) **487**, 77 (2012).

[17] Z. Fei, A. S. Rodin, G. O. Andreev, W. Bao, A. S. McLeod, M. Wagner, L. M. Zhang, Z. Zhao, M. Thiemens, G. Dominguez, M. M. Fogler, A. H. C. Neto, C. N. Lau, F. Keilmann, and D. N. Basov, Gate-tuning of graphene plasmons revealed by infrared nano-imaging, Nature (London) **487**, 82 (2012).

[18] A. N. Grigorenko, M. Polini, and K. S. Novoselov, Graphene plasmonics, Nat. Photon. **6**, 749 (2012).

[19] J. Kim, H. Son, D. J. Cho, B. Geng, W. Regan, S. Shi, K. Kim, A. Zettl, Y.-R. Shen, and F. Wang, Electrical control of optical plasmon resonance with graphene, Nano Lett. **12**, 5598 (2012).

[20] V. W. Brar, M. S. Jang, M. Sherrott, J. J. Lopez, and H. A. Atwater, Highly confined tunable mid-infrared plasmonics in graphene nanoresonators, Nano Lett. **13**, 2541 (2013).

[21] T. Stauber, Plasmonics in Dirac systems: From graphene to topological insulators, J. Phys.: Condens. Matter **26**, 123201 (2014).

[22] D. Rodrigo, A. Tittl, O. Limaj, F. J. García de Abajo, V. Pruneri, and H. Altug, Double-layer graphene for enhanced tunable infrared plasmonics, Light Sci. Appl. **6**, 16277 (2017).

[23] B. Yao, Y. Liu, S.-W. Huang, C. Choi, Z. Xie, J. Flor Flores, Y. Wu, M. Yu, D.-L. Kwong, Y. Huang, Y. Rao, X. Duan, and C. W. Wong, Broadband gate-tunable terahertz plasmons in graphene heterostructures, Nat. Photon. **12**, 22 (2018).

[24] A. Scholz, T. Stauber, and J. Schliemann, Plasmons and screening in a monolayer of MoS_2, Phys. Rev. B **88**, 035135 (2013).

[25] Y. Wang, J. Z. Ou, A. F. Chrimes, B. J. Carey, T. Daeneke, M. M. Y. A. Alsaif, M. Mortazavi, S. Zhuiykov, N. Medhekar, M. Bhaskaran, J. R. Friend, M. S. Strano, and K. Kalantar-Zadeh, Plasmon resonances of highly doped two-dimensional MoS_2, Nano Lett. **15**, 883 (2015).

[26] A. K. Mishra, S. K. Mishra, and R. K. Verma, Graphene and beyond graphene MoS_2: A new window in surface-plasmon-resonance-based fiber optic sensing, J. Phys. Chem. C **120**, 2893 (2016).

[27] T. Low, R. Roldán, H. Wang, F. Xia, P. Avouris, L. M. Moreno, and F. Guinea, Plasmons and Screening in Monolayer and Multilayer Black Phosphorus, Phys. Rev. Lett. **113**, 106802 (2014).

[28] D. Correas-Serrano, J. S. Gomez-Diaz, A. A. Melcon, and A. Alù, Black phosphorus plasmonics: Anisotropic elliptical propagation and nonlocality-induced canalization, J. Opt. **18**, 104006 (2016).

[29] Z. Liu and K. Aydin, Localized surface plasmons in nanostructured monolayer black phosphorus, Nano Lett. **16**, 3457 (2016).

[30] A. Nemilentsau, T. Low, and G. Hanson, Anisotropic 2D Materials for Tunable Hyperbolic Plasmonics, Phys. Rev. Lett. **116**, 066804 (2016).

[31] C. Gong, L. Li, Z. Li, H. Ji, A. Stern, Y. Xia, T. Cao, W. Bao, C. Wang, Y. Wang, Z. Q. Qiu, R. J. Cava, S. G. Louie, J. Xia, and X. Zhang, Discovery of intrinsic ferromagnetism in two-dimensional van der Waals crystals, Nature (London) **546**, 265 (2017).

[32] B. Huang, G. Clark, E. Navarro-Moratalla, D. R. Klein, R. Cheng, K. L. Seyler, D. Zhong, E. Schmidgall, M. A. McGuire, D. H. Cobden, W. Yao, D. Xiao, P. Jarillo-Herrero, and X. Xu, Layer-dependent ferromagnetism in a van der Waals crystal down to the monolayer limit, Nature (London) **546**, 270 (2017).

[33] G. Armelles, A. Cebollada, A. García-Martín, and M. U. González, Magnetoplasmonics: Combining magnetic and plasmonic functionalities, Adv. Opt. Mater. **1**, 10 (2013).

[34] P. Ares, F. Aguilar-Galindo, D. Rodríguez-San-Miguel, D. A. Aldave, S. Díaz-Tendero, M. Alcamí, F. Martín, J. Gómez-Herrero, and F. Zamora, Mechanical isolation of highly stable antimonene under ambient conditions, Adv. Mater. **28**, 6332 (2016).

[35] X. Wu, Y. Shao, H. Liu, Z. Feng, Y. L. Wang, J. T. Sun, C. Liu, J. O. Wang, Z. L. Liu, S. Y. Zhu, Y. Q. Wang, S. X. Du, Y. G. Shi, K. Ibrahim, and H. J. Gao, Epitaxial growth and air-stability of monolayer antimonene on $PdTe_2$, Adv. Mater. **29**, 1605407 (2017).

[36] G. Pizzi, M. Gibertini, E. Dib, N. Marzari, G. Iannaccone, and G. Fiori, Performance of arsenene and antimonene double-gate MOSFETs from first principles, Nat. Commun. **7**, 12585 (2016).

[37] M. Zhao, X. Zhang, and L. Li, Strain-driven band inversion and topological aspects in antimonene, Sci. Rep. **5**, 16108 (2015).

[38] A. N. Rudenko, M. I. Katsnelson, and R. Roldán, Electronic properties of single-layer antimony: Tight-binding model, spin-orbit coupling, and the strength of effective Coulomb interactions, Phys. Rev. B **95**, 081407 (2017).

[39] P. Ares, J. J. Palacios, G. Abellán, J. Gómez-Herrero, and F. Zamora, Recent progress on antimonene: A new bidimensional material, Adv. Mater. **30**, 1703771 (2017).

[40] A. V. Lugovskoi, M. I. Katsnelson, and A. N. Rudenko, Electron-phonon properties and superconductivity of doped antimonene, arXiv:1806.08203.

[41] L. W. Molenkamp, G. Schmidt, and G. E. W. Bauer, Rashba Hamiltonian and electron transport, Phys. Rev. B **64**, 121202 (2001).

[42] X. F. Wang, Plasmon spectrum of two-dimensional electron systems with Rashba spin-orbit interaction, Phys. Rev. B **72**, 085317 (2005).

[43] M. Graf and P. Vogl, Electromagnetic fields and dielectric response in empirical tight-binding theory, Phys. Rev. B **51**, 4940 (1995).

[44] F. Stern, Polarizability of a Two-Dimensional Electron Gas, Phys. Rev. Lett. **18**, 546 (1967).

[45] T. Low, F. Guinea, H. Yan, F. Xia, and P. Avouris, Novel Midinfrared Plasmonic Properties of Bilayer Graphene, Phys. Rev. Lett. **112**, 116801 (2014).

[46] O. V. Gamayun, Dynamical screening in bilayer graphene, Phys. Rev. B **84**, 085112 (2011).

[47] S. Tanuma, C. J. Powell, and D. R. Penn, Use of sum rules on the energy-loss function for the evaluation of experimental optical data, J. Electron Spectrosc. Relat. Phenom. **62**, 95 (1993).

[48] E. H. Hwang and S. Das Sarma, Dielectric function, screening, and plasmons in two-dimensional graphene, Phys. Rev. B **75**, 205418 (2007).

[49] K. Andersen and K. S. Thygesen, Plasmons in metallic monolayer and bilayer transition metal dichalcogenides, Phys. Rev. B **88**, 155128 (2013).

[50] D. A. Prishchenko, V. G. Mazurenko, M. I. Katsnelson, and A. N. Rudenko, Coulomb interactions and screening effects

in few-layer black phosphorus: A tight-binding consideration beyond the long-wavelength limit, 2D Mater. **4**, 025064 (2017).

[51] M. P. Marder, *Condensed Matter Physics*, 2nd ed. (Wiley, Hoboken, NJ, 2010).

[52] A. vom Felde, J. Sprösser-Prou, and J. Fink, Valence-electron excitations in the alkali metals, Phys. Rev. B **40**, 10181 (1989).

[53] R. Schuster, R. Kraus, M. Knupfer, H. Berger, and B. Büchner, Negative plasmon dispersion in the transition-metal dichalcogenide $2H$-$TaSe_2$, Phys. Rev. B **79**, 045134 (2009).

[54] J. van Wezel, R. Schuster, A. König, M. Knupfer, J. van den Brink, H. Berger, and B. Büchner, Effect of Charge Order on the Plasmon Dispersion in Transition-Metal Dichalcogenides, Phys. Rev. Lett. **107**, 176404 (2011).

[55] Z. H. Tao, H. M. Dong, Y. F. Duan, and F. Huang, Novel plasmonic modes of monolayer MoS_2 in the presence of spin-orbit interactions, Preprints **2018**, 2018070234.

[56] V. M. Agranovich and Y. N. Gartstein, Spatial dispersion and negative refraction of light, Phys. Usp. **49**, 1029 (2006).

[57] E. Feigenbaum, N. Kaminski, and M. Orenstein, Negative dispersion: A backward wave or fast light? Nanoplasmonic examples, Opt. Express **17**, 18934 (2009).

[58] P. J. Compaijen, V. A. Malyshev, and J. Knoester, Engineering plasmon dispersion relations: hybrid nanoparticle chain-substrate plasmon polaritons, Opt. Express **23**, 2280 (2015).

[59] D. Zhang, W. Lou, M. Miao, S.-C. Zhang, and K. Chang, Interface-Induced Topological Insulator Transition in GaAs/Ge/GaAs Quantum Wells, Phys. Rev. Lett. **111**, 156402 (2013).

[60] J. Kim, S. S. Baik, S. H. Ryu, Y. Sohn, S. Park, B.-G. Park, J. Denlinger, Y. Yi, H. J. Choi, and K. S. Kim, Observation of tunable band gap and anisotropic Dirac semimetal state in black phosphorus, Science **349**, 723 (2015).

[61] V. Sadovnichy, A. Tikhonravov, V. Voevodin, and V. Opanasenko, Lomonosov: Supercomputing at Moscow State University, in *Contemporary High Performance Computing: From Petascale toward Exascale*, edited by J. S. Vetter (CRC Press, Boca Raton, FL, 2013), pp. 283–307.